Selective laser sintered bio-inspired silicon-wollastonite scaffolds for bone tissue engineering

Nikhil Kamboj[1*], Jekaterina Kazantseva[2], Ramin Rahmani[1],

Miguel A. Rodríguez[3], Irina Hussainova[1*]

[1] Tallinn University of Technology, Department of Mechanical and Industrial Engineering, Ehitajate 5, 19086 Tallinn, Estonia

[2] Center of Food and Fermentation Technologies, Akadeemia tee 15A, 12618 Tallinn, Estonia

[3] Instituto de Cerámica y Vidrio (ICV-CSIC), C/Kelsen, 5, 28049 Madrid, Spain

ABSTRACT

The scaffolds, which morphologically and physiologically mimic natural features of the bone, are of high demand for regenerative medicine. To address this challenge, we have developed innovative bioactive porous silicon- wollastonite substrates for bone tissue engineering. Additive manufacturing through selective laser melting approach has been exploited to fabricate scaffolds of different architecture. Unique material combining osteoinductivity with osteoconductivity and biodegradability allows flexibility in design. As the porous structure is required for the ingrowth of the bone tissue, the CAD designed scaffolds with pore size of 400 μm and hierarchical gradient of pore size from 50 μm to 350 μm have been 3D printed and tested in vitro. The scaffolds have demonstrated not only the enhanced viability and differential patterning of human mesenchymal cells (hMSC) guided by the biomimetic design onto extra and intra scaffold space but also promoted the osteogenic differentiation in vitro. The scaffolds has shown the differential expression of primary transcription factors (RUNX2, OSX), anti-inflammatory factors and cytokines, which are important for the regulation of ossification; with RUNX2 and OSX expressed almost twice in hierarchically structured substrates as compared to homogeneous ones. The effective elastic modulus and compressive strength of scaffolds have been calculated as 1.1 ± 0.9 GPa and 37 ± 13.5 MPa with progressive failure for homogeneous structured scaffold; and 1.8 ± 0.9 GPa and 71 ± 9.5 MPa for gradient-structured scaffold with saw-tooth fracture mode and sudden incognito failure zones. The finite element analysis reveals more bulk stress onto the gradient scaffolds when compared to the homogeneous counterpart. The findings demonstrate that as-produced composite ceramic scaffolds can pave the way for treating specific orthopaedic defects by tailoring the design through additive manufacturing.

Keywords: Additive manufacturing; Scaffolds; Biomimetic design; Porous silicon; Wollastonite; Bone; Finite element analysis; Ossification

1. Introduction

The fusion of additive manufacturing (AM) with tissue engineering has revolutionized the production of novel customized scaffolds. A biomimetic approach to design a substrate inspired by a bone structure combined with capability of the AM to create complex architectures allow fabrication of constructs applicable for tissue engineering and regenerative medicine. With AM as a manufacturing tool and advanced methods of synthesis, the novel composite materials of tailored geometry and properties can be successfully produced to overcome limitations in medicine, renewable energy, and many other fields. In particular, the expansion of AM technology to bone tissue engineering has resulted in production of free-form porous scaffolds of well-controlled pore size, shape and volume without sacrificing the mechanical performance.

Bone performance can be characterized in terms of geometry, stiffness and toughness due to the hierarchical organization of the structure, which has been perfectly elaborated by nature. Therefore, there are certain requirements for the scaffold to be ideally applied for bone tissue engineering. The predominant objective of the scaffold is to mimic the natural features of the bone; the substrate should be biocompatible, bioactive and biodegradable, osteconductive and osteoinductive, providing open porosity, while possessing suitable strength and toughness to facilitate bone repair through remodelling and regeneration [1]. Consequently, an impeccable scaffold or biomaterial should not only act as a matrix promoting the osteoblast adhesion but also regulate the biochemical signalling pathways simulating the osteoblast behaviour for bone tissue engineering [2]. Moreover, a versatile scaffold shaped by additive manufacturing techniques can closely fit into the patient's body to heal either long size or critical sized defects.

A wide variety of biomaterials for bone tissue engineering has recently been developed. Amongst them, there are metallic, ceramics, polymeric and composite scaffolds. The most commonly used metallic scaffolds encircled around stainless steel and titanium-based and metal matrix based biomaterials. However, their low degradability and resorption, relatively high stiffness and stress-shielding phenomenon impede a native tissue from mechanical stimulation [3]. On the counterpart various natural and synthetic clustering ceramics and polymers, have been extensively used. The ceramics and polymers attempt to fulfil the gap left by metallic scaffolds by exhibiting good degradability, biocompatibility, controlled resorption for consecutive neoformation of the bone, and untroublesome tampering in the degradation through copolymerisation and changes in hydrophobicity and crystalline structure [3]. Nonetheless, the single phase scaffold comprising either ceramic or polymer material limits the applications to non-loading bearing applications and non-critical sized defects.

In order to unravel the problem, various bio-composites have been tested. The primary objective of the composite scaffold is to coalesce two or more materials to improve the printability of the constructs with tailored architecture and required mechanical performance [4]. Wollastonite, a naturally occurring calcium silicate mineral, has been extensively used as an active filler in both ceramic-ceramic and ceramic-polymer composites due to the mechanical properties, which can be accredited to its acicular structure, and its ability to hamper the fracture by impeding the crack pathway [5]. The hydrophilic nature of the wollastonite facilitates the formation of the apatite layer promoting wollastonite usage for bone tissue regeneration. Moreover, the early stage lixiviated calcium ions from wollastonite regulate the osteoblast proliferation and differentiation [6] and have the potential to upregulate several bone markers genes expression of the stem cells such as BMP-2, RUNX2 gene, transforming growth factor (TGF-β), ALP and osteocalcin *in-vitro*. Ions of silicon are not only involved into secretion of extracellular matrix, but also play a crucial role in activation or de-activation of mitogen-activated protein kinase (MAPK) MAPK/ERK and MAPK/p38 signalling pathway [7]. Additionally, wollastonite based silicate materials may influence the regulation of immunomodulation causing the downregulation of the inflammatory MAPK and NF- κB signalling pathways and the upregulation of the apoptosis of macrophages by a caspase-dependent pathway [8].

Wollastonite added ceramic-polymer composites, which were explored as the potential orthopaedic implants, are mostly fabricated with the help of physicochemical and thermomechanical methods, which are constrained in freedom of design. Over the past few years, additive manufacturing has been used as a tool to fabricate the wollastonite-based composites for bone tissue engineering. Recently, the "diamond cell" architectured wollastonite-diopside glass-ceramics biocomposites were produced by digital light processing (DLP) with [9] apatite-wollastonite reinforced PLLA matrix scaffolds was fabricated using a fused filament approach [10]. The new dilute Mg-doping β phase of wollastonite scaffolds was prepared by direct ink writing [11]. The apatite-wollastonite-poly (lactic acid) scaffolds was fabricated by two step technology comprising 3D printing of PLA matrix which was subsequently followed by thermal treatment to form hybrid material [12]. The bioactive wollastonite and wollastonite-based composites have the property of osteoconduction and bonding with the living bone tissue by the so-called process of "bonding osteogenesis". However, the bioactivity is not only the important key factor to determine the ideal scaffold but also it should possess good degradability and osteoinductive properties too. The scaffolds for

the bone repair should degrade over the passage of time; and the degradation should be neither too fast [13] nor too slow [14].

One of the osteoinductive and biodegradable materials, which is used over the past two decade, is porous silicon, as silicon plays a crucial rule in the development and nourishment of the bone. Silicon matrix is well sustained in the human body with neither inflammatory nor infectious reactions of the host. Additionally, the porous silicon matrix, when hydrolysed by body fluids, is converted to non-toxic silicic acid - the major form of silicon in the human body [15] and may be beneficial for creation of a cell interface to support osteoblast and collagen fibrils [16] and inhibition of osteoclasts development and bone resorption activities [17]. Porous silicon is also proven to play a vital role in assisting and promoting the formation of the actin microfilaments from the stem cells [18]. Pairing of porous silicon and human mesenchymal cells (hMSC) has led to various therapeutic effects for the regenerative medicine and personalized medicine, which can be attributed to the ability of MSC to differentiate and self-renew to multiple tissues [16,19,20].

Tailoring the pore morphology, porosity and size can affect the physiological fluid rate; particle size distribution can hamper extracellular enzyme activity, divergent gene expression; and crystallinity can alter intercellular activity. For instance, tuning of the pore size of porous silicon has resulted in differential expression of bone marker genes and neuronal associated genes [21]. The micropores of 10-50 μm are required for physiological fluid infiltration, cell adhesion, rapid exchange and diffusion of oxygen and nutrients and waste clearance [22]. The macropores sizes from 100 to 400 μm are needed for the cell infiltration and building of new bone tissue layers [22,23]. The porous silicon matrix has been usually fabricated by conventional anodization and stain etching methods for porosification. The laser-assisted approaches combined with precise bioinspired design have never been reported in the literature.

In this work, the approach of additive manufacturing through a selective laser melting (SLM) as an effective technique to fabricate a novel metalloid/ceramic composite scaffold is used for the first time. Unique material combining bioresorability, osteoinductivity with osteoconductivity and biodegradability is developed allowing flexibility in design and lack of volumetric shrinkage. The material of macro-porous silicon reinforced by bioactive acicular wollastonite, which is produced with customized complex geometry and porosity, is an effective solution for bone tissue engineering. Homogeneous and gradient scaffolds of distinct geometries, which previously could not be easily engineered, were designed to mimic the microenvironment of the bone. For instance, structural gradient of the radially distributed pores can facilitate a long bone formation; whereas the axially distributed pores can enhance a flat
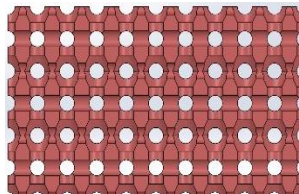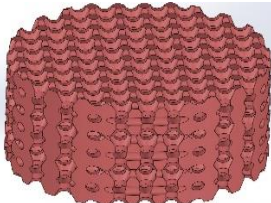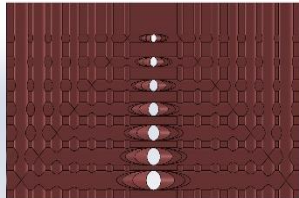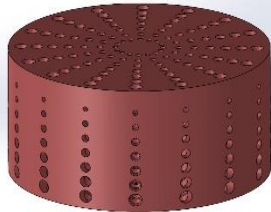
bone formation [22]. The gradient scaffold not only improve the cell-seeding efficiency, but also assist the osteogeneic differentiation due to availability of nutrients and subsequent tissue development [24].This kind of fabrication technology with biomimetic design for homogeneous and gradient scaffolds can further guide the stem cells behaviour to the differential expression of the biological signalling molecules.

2. Experimental

2.1 Scaffolds design

To fabricate three-dimensional scaffolds of 6 mm in height and 5 mm in diameter, a computer aided design was sketched with the pore diameters for the homogeneous(H) scaffolds to be 400 µm and the gradient scaffolds(G) from 50 µm to 350 µm using SOLIDWORKS® (Dassault Systems, USA) as shown in Table 1.

Table 1. Morphology and CAD 3D design of the scaffolds

Type of scaffold	Pore size	Designed pores	CAD 3D design
Homogenous (H)	400 µm		
Gradient (G)	50 µm ↓ 350 µm		

2.2 Powder feedstock

The material used was a mixture of 30 wt% silicon and 70 wt% wollastonite. The powders of silicon (>99.9% purity, particle size range 10 - 44 μm, *Silgrain-Elkem*, Fig 1a) and wollastonite (>99.9% purity, particle size range 1–10 μm, *NYCD® M1250*, Fig. 1b) were mixed in the Turbula® shaker for 3 h with ethanol using ZrO_2 balls. The obtained mixture was dried in an oven heated to 120 °C for 24 h.
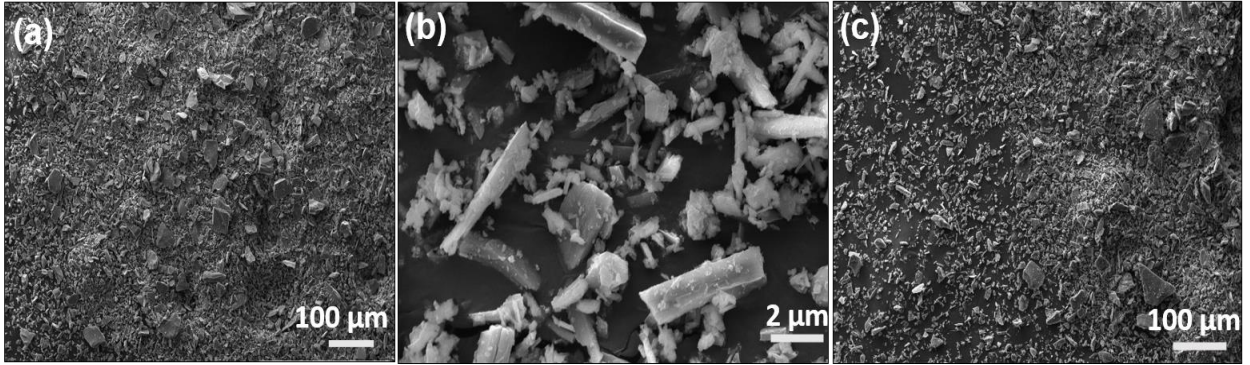
Fig. 1. Microstructure of the precursor powders: a) silicon; b) acicular wollastonite; c) mixed powder

2.3 Processing

Scaffolds were fabricated by metal 3D printer using a commercial ReaLizer GmbH SLM-50, Germany, SLM system. The optimized process parameters were applied for production of the porous substrates with layer thickness of 25 μm, hatch distance of 60 μm, and point distance of 10 μm at a scanning speed of 80 mm/s. Additionally, the macroporous silicon scaffolds of the same CAD design were manufactured exploiting the process parameters as specified in Table 2. The procedure was performed under the high purity argon (99.999 vol%) in order to avoid undesirable oxidation. During SLM, a rubber wiper spreads the composite powder feedstock over the surface of a stainless steel cylindrical platform. No post-treatment of the sintered materials was required after SLM, which ultimately reduces the cost of the whole process. The loose powder adhered to the scaffolds was removed by a sonicator kept in ethanol for 15 minutes.

Table 2. *Process parameters*

Samples	Laser power (W)	Energy density (J/mm^3)
Macroporous silicon	34	283
Bulk composite	32	267
(H) and (G) scaffolds	26	217

2.4 Microstructural analysis

Phase composition of the crushed scaffolds was evaluated by X-ray diffraction (XRD; D5005, Bruker, USA) operating at CuKα1 radiation ($\lambda = 1.5406$ Å) with a step of 0.02° (2θ) in the range of 20° - 70° with the assessment and optimization of the relative counts by Rietveld refinement method. Scanning electron microscopy (SEM Zeiss EVO MA 15, Germany) equipped with EDS with a voltage of up to 20 kV and magnifications up to 50 kX was used for examination

of the as-produced products. The gold-coated samples were studied under secondary and backscattered electrons modes. The front and cross section details of the scaffolds were examined using MEDIX technology MXT 225 HU-CT machine. A rotational step of 0.9° over an angle of 180° was imposed to obtain the images of the scaffolds. The images of the (H) and (G) scaffolds were taken from three different samples of each type. The visualization and 3D representation of the scaffold were performed through μ-CT analyser. The scaffolds were reconstructed comprising 120 slices using a circular region of interest (ROI). Subsequently, the identical threshold values were defined for the same region of (H) and (G) scaffolds in all three different samples of each type in-order to minimize the image noise and differentiate between the dense materials from pores. The threshold values were reformulated and inverted to obtain the porosity of the scaffolds.

2.5 Compression tests

The cylindrical porous samples of 6 mm (±0.1 mm) in diameter and 5 mm (±0.1 mm) in height were tested under compression at room temperature at an applied strain rate of 0.5 mm min^{-1} using the servo-hydraulic model 8500 universal testing machine (Instron ltd., UK). The compressive load and displacement were recorded at each 0.1 s intervals during testing. Elastic modulus and maximum compressive strength were determined using software associated with the testing machine.

The mechanical performance of the structures was also evaluated computationally using a finite element (FE) analysis. Modelling was carried out on the scaffolds with a constant deformation rate of 0.5 mm min^{-1} in order to be consistent with the experimental compression uniaxial deformation. The commercial FE ANSYS® 17.2 package was used for the estimation of a local stress distribution. The 10 noded tetrahedral elements were introduced in order to achieve the fine mesh structure.

2.5 Cell cultures and cell staining

Human MSCs were obtained from a freshly isolated subcutaneous adipose tissue as detailed in [25]. Cells were grown in DMEM with 10% FBS, 1 mg/ml penicillin and 0.1 mg/ml streptomycin at 37 °C in 5% CO_2. UV-C treatment was imparted to the scaffolds to prevent any contamination to the cell culture. The scaffolds were infiltrated with nutrients from DMEM consecutively three times in the passage of 24 hours prior to cell seeding in order to saturate the scaffolds with the active components from the medium.

The hMSCs were seeded on the surface of the scaffolds in 12-well plate at 4×10^4 per well, correspondently. On the counterpart, similar cells were grown on the flat glass with the same culture condition to be used as the control and reference. The visualization of the cells adhered onto the scaffolds was performed using a specific to filamentous actin (F-actin) phalloidin tagged by FITC (Sigma). The cells were fixed by 4% PFA at 48 h after seeding, washed by PBS and permeabilized by 0.3% TRITON X-100 in PBS for 5 minutes. The scaffolds were kept for 18 hours at 4 °C, which allows Phalloidin-FITC (1:100) staining, and 2 hours at RT for cells cultured on the flat glass (control). For nucleus staining, cells were incubated with Hoechst 33342 (Invitrogen, 1 µg/ml) for 10 minutes. After a final PBS wash, the phalloidin-stained cells were analysed by Nikon Eclipse 80i microscope

2.6 RNA extraction, cDNA synthesis and RT-qPCR of osteogenic genes

RNAs were extracted directly from cells grown on the scaffolds by invitrogen kit according to the manufacturer's recommendations. The cDNAs were synthesized from 9.75 µl of DNase-treated (Ambion) RNA with 22.75 µl RevertAid Reverse Transcriptase (Thermo Fisher Scientific). The quality of the cDNA was affirmed by RT-PCR using GAPDH primers and HOT FIREpol® Master Mix (Solis Biodyne, Estonia). To evaluate the level of osteogenic differentiation, such kind of genes were analysed after 21 days: OCN, OPN, COL1a1, RUNX2, OSAD, ALP, MSX2, TFGβ, IL8 and TSG6. The experiments were performed in triplicates by using EvaGreen qPCR mix plus no Rox (Solis Biodyne, Estonia) and the StepOnePlus™ Real-Time PCR System (Thermo Fisher Scientific). The fold change of the gene taken into consideration was calculated relatively to the control (cells grown without scaffolds) after normalisation to GAPDH expression, using 2-ΔΔCt method (double difference of Ct). The values were respectively $\Delta Ct = Ct(\text{gene of interest}) - Ct(\text{GAPDH})$, and $\Delta\Delta Ct = \Delta Ct(\text{treated}) - \Delta Ct(\text{control})$ [26].

2.7 Statistical analysis

The values were presented as the mean ± SD and analyzed with Student's t-test, in which differences were considered statistically significant when $p < 0.05$.

3. Results and discussion
3.1 Silicon scaffolds

Fig. 2(a, b) shows the SLM fabricated porous silicon scaffold. The CAD designed pores of 400 µm are well recognized in the SEM images.
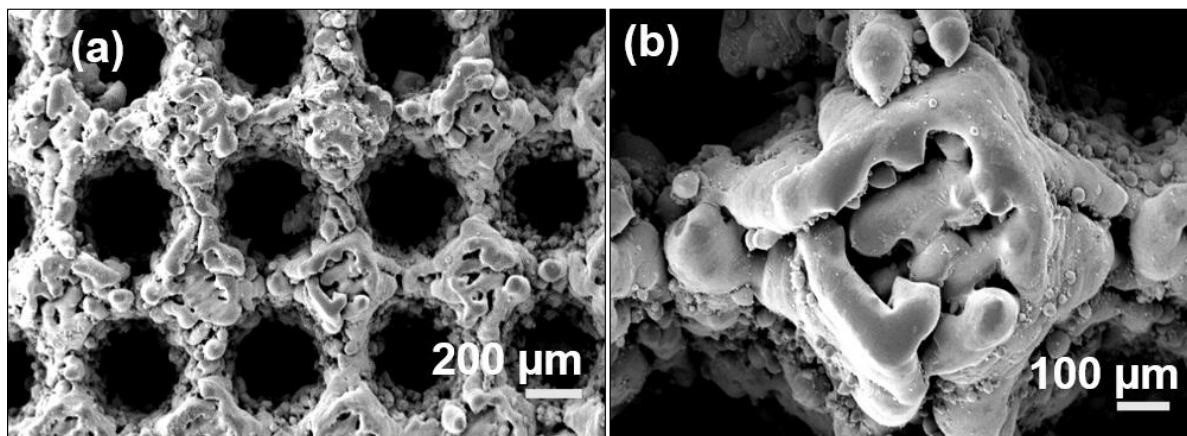
Fig. 2. SEM micrographs of macroporous silicon scaffolds

The morphology of the scaffolds depends on the process parameters (laser power and energy density) to a great degree. Recent study [27] has demonstrated that the laser power of 34 W with the energy density of 283 J/mm^3 is suitable for complete densification of the silicon powder by SLM. Herein, the laser current of 32 W with the energy density of 266 J/mm^3 was applied for fabrication of the silicon scaffolds with the pore size of 400 µm (Table 2) conditioned by the fact that a high laser energy can significantly reduce the viscosity of the molten silicon, which can readily flow to join the large droplets in the melt pool, and decrease the pore size in the construct. Furthermore, the Nd^{3+}: YAG laser contributes to the sintering of silicon particles and formation of a porous silicon matrix as shown in Figs. 2(a,b). The differential pattern of the silicon particles adhesion after the SLM processing and the intrinsic feature of the SLM technique imparts surface roughness on the scale of several micrometres [28].

The next step was to fabricate the silicon-wollastonite composite scaffold with a different geometrical design (H or G, Table 2) compatible for bone tissue engineering and taking into consideration the process parameters window working for SLM of the pure silicon.

3.2 Analysis of composition

After SLM processing, the main phases detected in the scaffolds were silicon [ICSD, 00-027-1402, cubic], wollastonite [ICSD, 04-016-5334, Triclinic] and pseudo-wollastonite [ICSD, 04-012-1776, Monoclinic]. In the previous study [29], the silicon-wollastonite based scaffolds with 50-wt% of each component have shown an evidently pronounced increase in the crystallinity of the phases after SLM as compared to the powder feedstock.

As it can be observed from Figs. 3(a,b) there is no noticeable difference in the phases presented in homogenous and gradient scaffolds suggesting the homogeneous mixtures of the powders, as well as repeatability and reproducibility of the process. The acicular wollastonite interaction with the Nd^{3+} YAG laser had led to a higher temperature polymorph of wollastonite or pseudo-wollastonite. The upper temperature stability of wollastonite is 1150 ^{0}C, and beyond that, there is a transition to pseudo-wollastonite phase. The pseudo-wollastonite can also be recognized in Figs. 3(a,b), which confirms the co-existence of wollastonite and pseudo-wollastonite. This can be attributed to the fact that the melt pool formed was not uniform, which was conditioned by irregular shaped powder particles. The wollastonite and pseudo-wollastonite phases were detected in both (H) and (G) scaffolds. In principal, the pseudo-wollastonite is considered as a promising material for bone generation and can enhance cell activity and osteoblast differentiation [30]. The difference between the phases is the crystal structure: a "three-ring silicate" crystal structure of a stable wollastonite as compared to a "chain-silicate" structure of unstable wollastonite, i.e. pseudo-wollastonite [31].
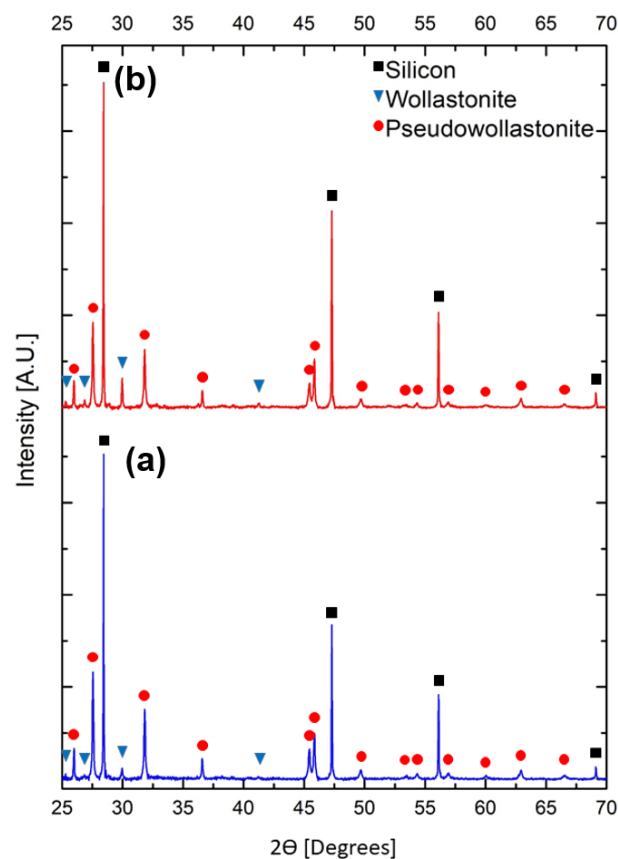

Fig. 3. XRD of the SLM processed crushed scaffolds; a) **(H)**; b) **(G)** scaffolds.

3.3 SLM fabricated composite scaffolds

Fig 4 represents the scaffolds design depicting its pore morphology and 3D models. The (H) scaffolds with pore size of 400 µm and (G) scaffolds with gradient pore size from 50 to 350 µm clearly replicated the scaffolds microstructure given in Figs. 4(a,d). The (G) scaffold was designed to have both radial and longitudinal gradient in pore size required for both long bones and flat bones, as small pores allow high vascularization and large pores facilitate direct osteogenesis and formation of the multiple tissues and tissue interfaces [22].

The gradient in (G) scaffold longitudinal pore size is demonstrated in Fig.4(d). The pores connectivity is slightly different in (G) and (H) scaffolds. Representative SEM images of (H) scaffolds in Figs. 4(a,c) shows the continuous connectivity of at least four macropores with the interconnected strut as observed in the porous silicon scaffolds in Fig. 2b. On the counterpart, the pores of the gradient scaffolds are not connected being separated in longitudinal and radial direction (Fig 4(d)).

Wollastonite is quite homogeneously dispersed throughout silicon as depicted by the EDS elemental mapping, which displays Si in green and calcium in red, Figs. 4(b,e).

Figs. 4(c,f) show the µ-CT images of the (H) and (G) scaffolds with the macropores, respectively. The composition of silicon and wollastonite was opted since silicon being osteoconductive and osteoinductive and wollastonite imparts bioactivity to the scaffold. For (H) and (G) scaffolds, the µ-CT of the five samples were taken into consideration and a total porosity of 41 vol% and 30 vol% was measured, correspondingly. The pores gradient from the small to larger ones is demonstrated with the help of a red arrow in µ-CT image of the (G) scaffold, Fig. 4(f). The supremacy of the SLM technique as compared to other AM approaches can be accredited to the fabrication of substrates with different porosity, controllable pore size, no binder addition and no post-processing stages. Furthermore, removal of binder, geometric constraints, sintering and other additional treatment steps are not only time consuming, but also affects the degradation of physical-chemical characteristics of the as-produced porous scaffolds.
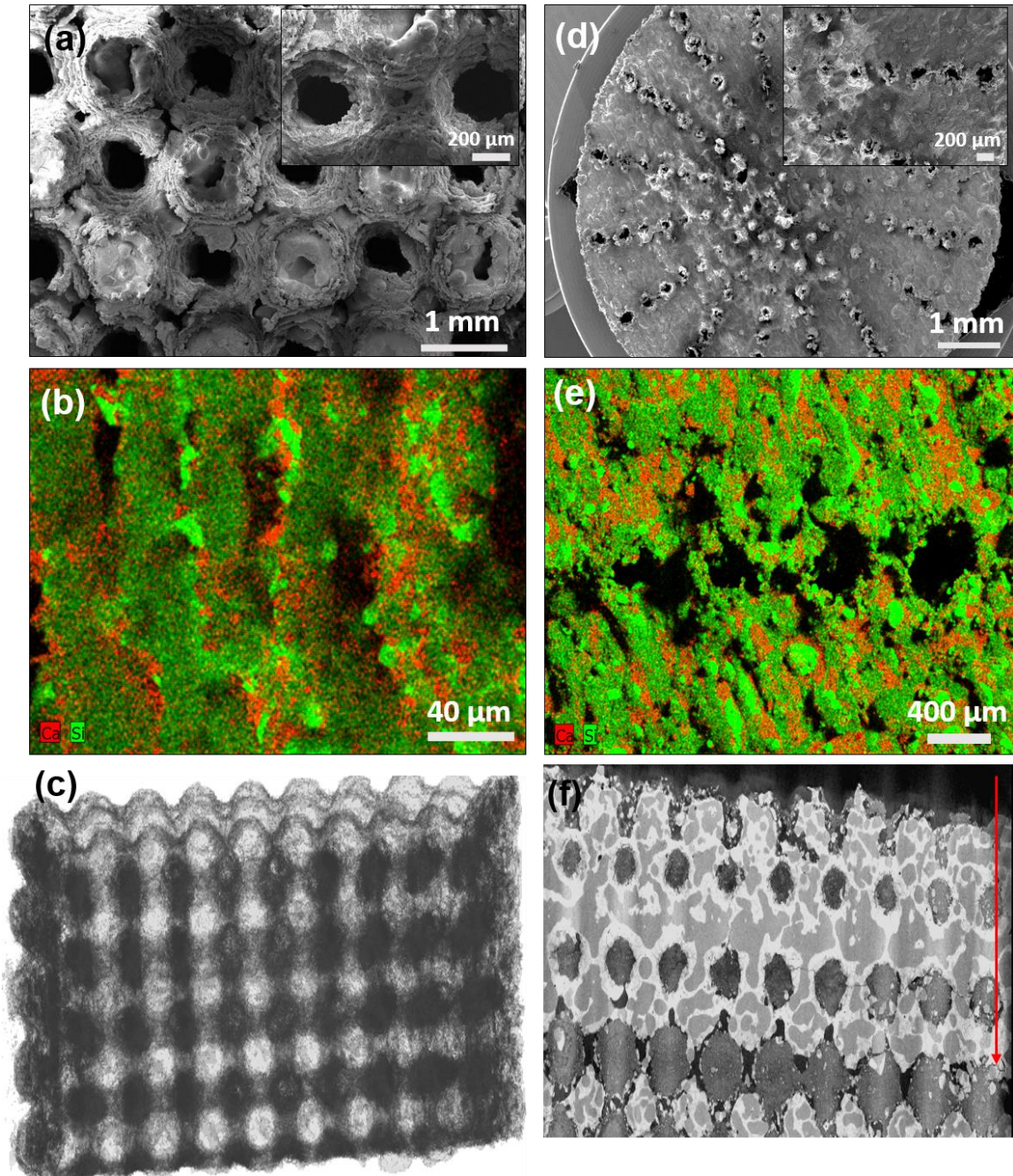
Fig. 4. **(H)** a) SEM micrographs of the (H) scaffolds; b) EDS element mapping of the (H) scaffold; c) μ-CT image of the (H) scaffold; **(G) d**) SEM micrographs of the (G) scaffold; e) EDS element mapping of the (G) scaffold; f) μ-CT image of the (G) scaffold

3.4 Silicon matrix containing acicular wollastonite

Fig. 5 demonstrates the localization of silicon and wollastonite particles throughout the (H) scaffold and a bulk comprising the same composition. Relatively large areas of Si can be attributed to much more likely laser interaction with the large particles (silicon) than with smaller acicular particles (wollastonite).
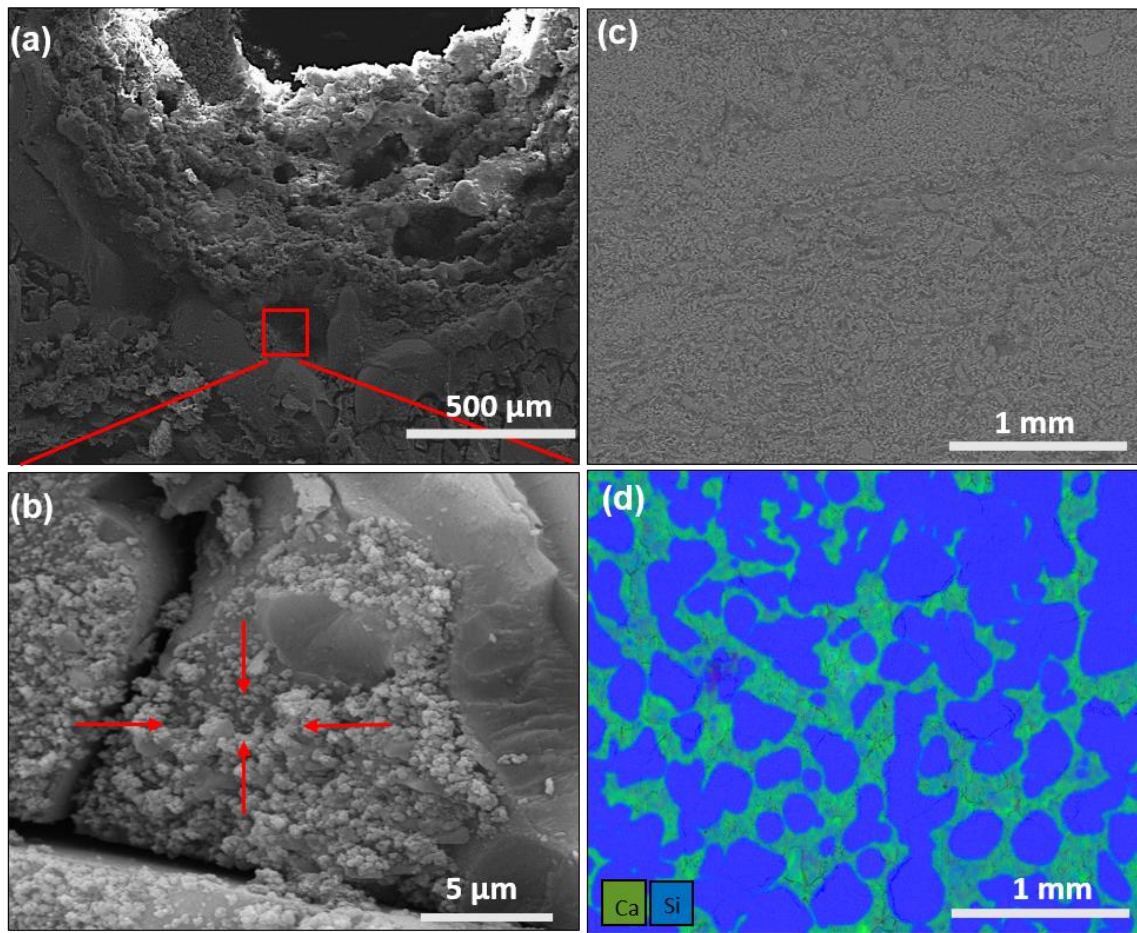
Fig. 5. Schematic representation and mechanism of the produced silicon-wollastonite scaffolds by SLM; a) and b) (H) scaffold; c) and d) bulk composite

The wollastonite particles are clearly recognizable being embedded onto the silicon matrix as indicated by arrows in Fig.5(b). The bioactive particles of wollastonite are supposed to leach in the body fluids first. The authors' study [29] has indicated the degradation of as-fabricated scaffolds with 50 wt.% of each component and revealed that the Ca / Si ratio was 1.60 after the first day of the test, and decreased to 0.65 after the 14th day. Such kind of behaviour suggests the release of wollastonite in Tris buffer, which evidences the attachment of wollastonite to the particles onto the silicon matrix. The high magnification image in Fig. 5(b) displays the relatively homogenous distribution of wollastonite particles on the matrix' silicon, which may be accredited to robust convention muster by rapid heating and solidification. It is worth mentioning that the top layer of the SLM printed bulk exposed the microstructure with heterogeneous grain boundaries of the silicon particles rich with acicular wollastonite.

3.5 Compression test

In Fig. 6, the stress – strain curves of the structures developed are demonstrated. The stress-strain curves begin with a linear elastic response followed by nonlinear behaviour with the

13

applied stress. The plot depicted for (H) scaffold reveals a linear response until about 40 MPa followed by a multi-peaks profile, which is typical for cellular structures, Fig. 6a. The curve has a positive slope up to the highest stress of 37 MPa, and then gradually proceeds with a negative slope pointing at the cracks system development. The gradient scaffold (G) withstands twofold higher stress level linearly reaching 72 MPa, Fig. 6c. The effective elastic modulus and the compressive strength are calculated to be 1.1 ± 0.9 GPa and 37 ± 14 MPa for (H) scaffold; and 1.8 ± 0.9 GPa and 71 ± 10 MPa for (G) scaffold, respectively. The stress-strain response of the (H) scaffolds shows continuous progressive failure of the construct owing to its uniform and homogenously distributed pores. Correspondingly, the (G) scaffolds demonstrates the sudden "incognito" failure zone, which can be attributed to the fact of non-homogeneous stress distribution towards differently sized pores. Such kind of behaviour may have real implications when scaffolds are implanted for long or flat bones restitution since the gradient in porosity can support the interphase separating the dense from the porous part in the long bones axially and in the flat bones longitudinally.

The compressive strength of the as-fabricated scaffolds is greater than the strength of a trabecular bone (1-10 MPa) but less than the stress of a cortical bone (110-230 MPa). One of the remarkable features of the powder feedstock for the scaffolds of the developed composition is a flexibility in production of powders of the specified ratio of the components, which can be tailored for custom needs. For instance, the effective elastic modulus and compressive strength of 2.9 ± 0.3 GPa and 110 ± 5 MPa was measured for the material comprising 50 wt% of each component; therefore, such kind of materials may be considered as a promising candidate for treating the cortical bone defects [29].

Furthermore, the stress distribution was assessed by finite element analysis. The compressive force was uniaxial applied onto the top surface of the CAD model keeping the bottom fixed. The response of the structures were modelled in the linear portion of the stress-strain curve. The non-linear stress-strain section of the curve was not modelled since it leads to the reduction in the overall stress with the constant increase in the deformation. The non-linear stress - strain section of the curve evoked from 8% and 6% strain in (H) and (G) scaffold, respectively. The Figs. 6(b, d) illustrate the patterns of the stress distribution onto the (H) and (G) scaffolds under the constant deformation. The red spots or patches denote the most stressed areas; and the greenish yellow ones points to the stress concentration around the pores. The greenish blue contour corresponds to stress of ~ 47 MPa and ~ 77 MPa for homogeneous and gradient scaffolds, respectively. For both constructs, the least stress was observed at the middle region

and at the point of scaffold fixation to the support. The highest stress was concentrated at the surface of both scaffolds in a close proximity with the mesh.
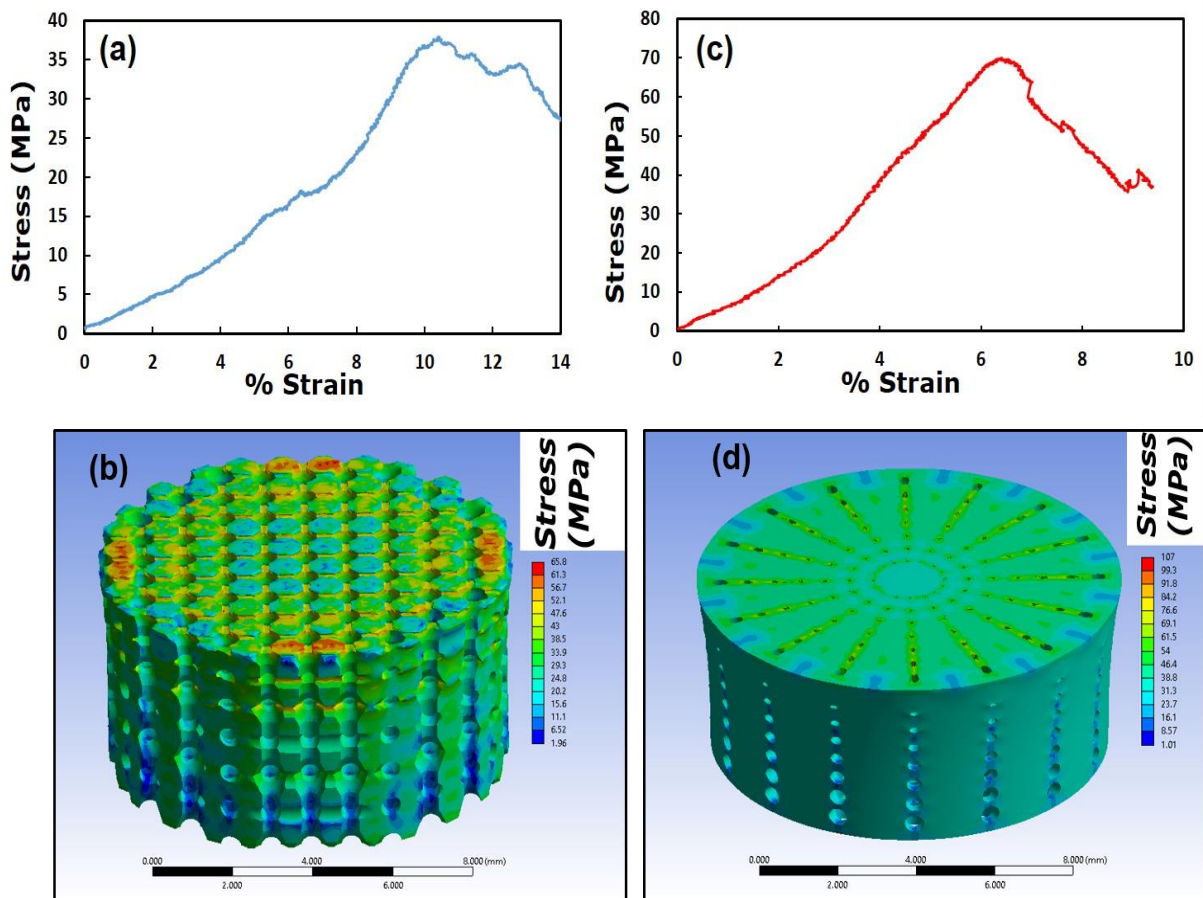

Fig. 6. a) and b) Experimental stress-strain response and finite element analysis of (H) scaffolds; c) and d) (G) scaffolds

3.6 Cytocompatibility assessment of the scaffolds

The most essential requisite for the scaffolds to be used in bone tissue engineering is a relevant biomaterial with a desired pore size. Both of the porous silicon wollastonite and pseudo-wollastonite scaffolds are considered as excellent substrates for the cell attachment and proliferation [16,30,31]. Figs. 7(c-f) shows that hMSCs are capable to grow on the silicon-wollastonite composite (H) scaffold, Fig. 7(c,d), and on the (G) scaffold, Figs. 7(e,f). Additionally, migration of the cells are vital that can change the cell density, oxygen and nutrient availability. These factors are seemed to be associated with the pore size [32]. The distinguishing feature of the hMSCs grown on the scaffolds and on the reference glass is the presence of pores and the complex 3D geometry affecting the stem cells morphology after 48 hours. The hMSC appeared to be well anchored to the (H) scaffolds, Figs.7(c,d).

The spindle shaped cells with more than usually extended cytoplasmic lamellopodia extensions were well-connected indicating a better initial cell attachment onto the 3D printed (H) scaffold. The extended morphology of the hMSC can be attributed to a siutable connectivity, which is one of the major pre-requisites for favoured osteo-lineage differentiation to extracellular matrix needed by osteoblasts to proliferate. It was observed that hMSCs were well-adhered onto the (G) scaffold surface (extra scaffold space) encircling and guided by the biomimetic design of the pores, Fig. 7e. The hMSC were seen communicating each other in the intra-scaffold space provided by the largest pores, Fig.7f. Cell migration in and out (from extra-scaffold space to intra-scaffold space) in the (G) scaffold through the pores sized from 100 μm to 350 μm can be beneficial for the bone tissue regeneration. The arrangement of the cells can facilitate the cell-surface interaction by promoting direct bonding and, therefore, enhance the bone tissue formation with profound media flow of nutrients allowing the differentiation of hMSC to osteoblast cells [32]. Additionally, it could affect cell behaviour in regard to extracellular matrix deposition and differentiation [33].
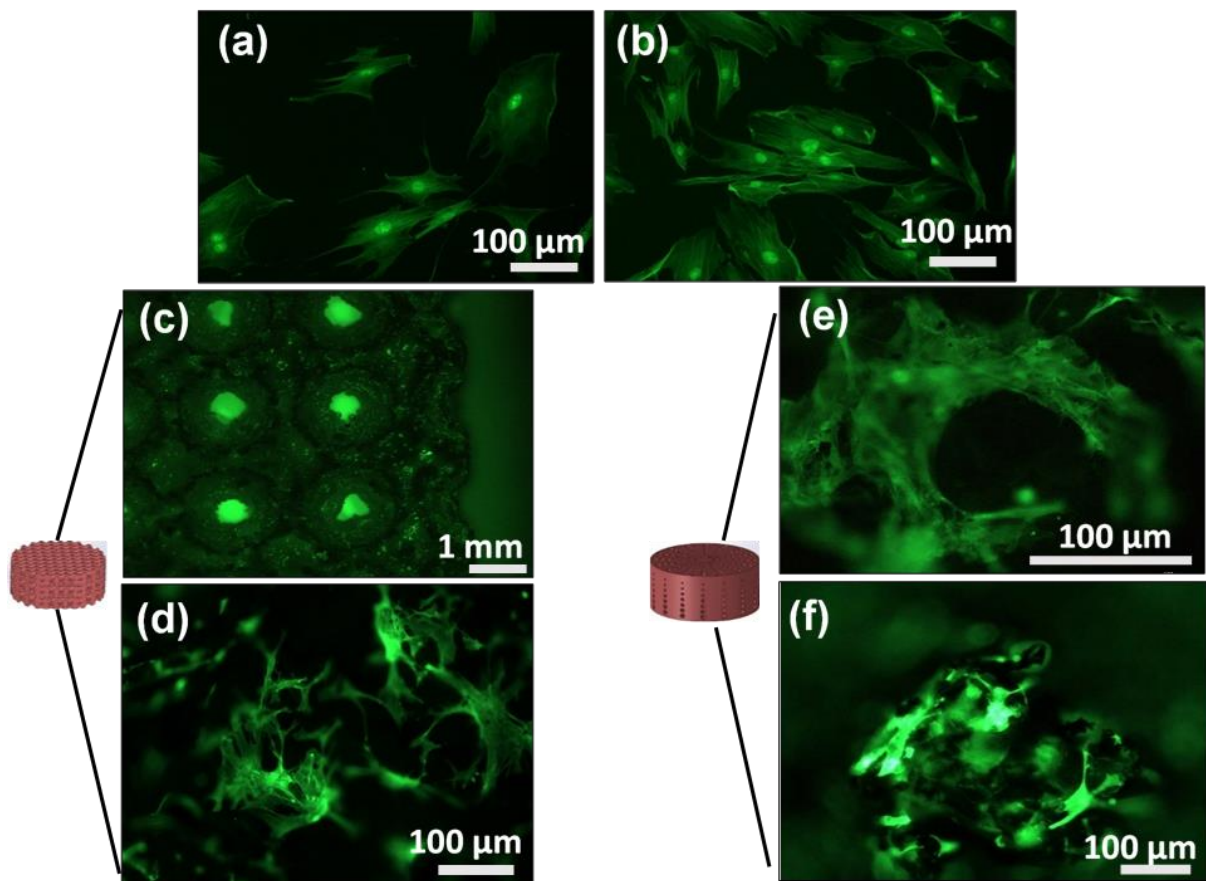

Fig.7. The fluorescence microscopy images of hMSCs grown on glass (a, b), (H) scaffolds (c, d) and (G) scaffolds (e, f).

3.7 Osteo-lineages studies

The induction of the osteogenic features by (H) and (G) scaffolds were evaluated by mRNA levels of RUNX2, OSX, osteocalcin, OSAD, BMP-2, Col1, ALP, MSX2, TSG6, TGβ1 and IL8 through MSC seeded onto the scaffolds microenvironment, Fig. 8. Analysis of the MSC was performed in the absence of either chemical or biological stimulus. Induction of the RUNX2 and OSX, the primary transcription factors for osteogenic differentiation, was found in both scaffolds. The expression of both transcription factors were expressed nearly twice in (G) scaffolds as compared to (H) scaffolds. The induction of the RUNX2 plays a pivotal and stimulatory role in the osteoblast differentiation. ALP, type I collagen (Col1a1), clearly shows the up-regulation of the relative expression in gradient scaffolds. Although the cell number seeded and the calcium production per volume onto the (H) and (G) scaffolds were not evaluated, the elevation of the certain early osteogenic transcription factors like RUNX2 and OSX can be observed in the gradient scaffold; and be attributed to re-distribution of the hMSC along the differential pores with a higher nutrient and oxygen availability as compared to (H) scaffolds.

The ossification is controlled not only by the transcription and mineralization factors, but also by certain cytokines such as TGFβ, IL8 and TSG6, which were also evaluated in this study. The relative expression of the cytokines was relatively similar in (H) and (G) scaffolds. The up-regulation of IL-8 and TGFβ, which are anti-inflammatory factors, demonstrates the possible immunomodulation effect. The induction of TSG6 in both scaffolds was considered advantageous as TSG-6 regulates the bone remodelling by maintaining the stasis between osteoblasts and osteoclasts.
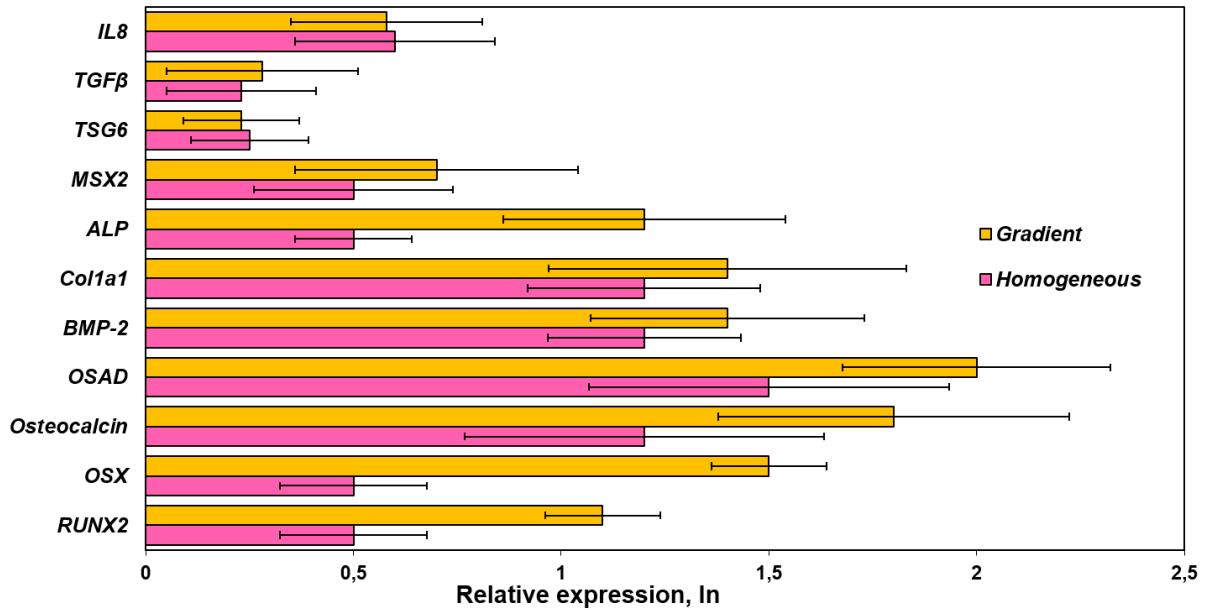
Fig. 8. Dynamic potential of MSC differentiation to osteo lineages by (H) and (G) scaffolds

4. Conclusions

For the first time, the novel powder feedstock combining osteoconductive, osteoinductive and bioactive elements was developed for 3D printing of the bio-mimetically designed scaffolds for bone engineering. The innovative metalloid/ceramic porous silicon-wollastonite substrates were additively manufactured exploiting the approach of the selective laser melting (SLM). The addition of silicon provided various advantages including (a) good absorptivity for the Nd:YAG laser; (b) osteoinductivity of the scaffold; (c) mechanical strength; (d) printability in single step technology; (e) bio-interface to support osteoblasts.

The parameters of SLM 3D printing were optimized in terms of laser power and energy density. The CAD designed scaffolds with pore size of 400 µm (H) possesses effective elastic modulus and compressive strength of 1.1 ± 0.9 GPa and 37 ± 13.5 MPa, respectively. The scaffolds with the hierarchical gradient of pore size from 50 µm to 350 µm (G) exhibit the effective elastic modulus and compressive strength of 1.8 ± 0.9 GPa and 71 ± 9.5 MPa, respectively.

The hMSC were well-anchoraged onto the (H) and (G) scaffolds. Differential pattern of the hMSC onto the (G) scaffolds was seen onto both extra- and intra- scaffold space guided by the biomimetic design.

Induction of the RUNX2 and OSX, the primary transcription factors for osteogenic differentiation, was expressed nearly twofold in (G) scaffolds as compared to the (H) scaffolds.

Induction of the IL-8 and TGFβ anti-inflammatory factors demonstrated the possible immunomodulation effect of the scaffolds.

Complex shaping of bio-ceramics is remained a challenge. The fabrication of the novel scaffolds can be envisioned to open avenues for a new powder feedstock to produce customized scaffolds by SLM process with flexibility in design and without any binder addition and post processing stages. The fabricated novel metalloid/ceramic porous silicon - wollastonite scaffolds not only provide an immediate support to the bone tissue providing a subsequent release of the wollastonite to the body fluids, but also give the ability to deliver biological moieties for the treatment of bone infection.

5. Declaration of Competing Interest

The authors declare that they have no known competing interests.

6. Acknowledgements

7. References

1   C. Xu, P. Su, X. Chen, Y. Meng, W. Yu, A. P. Xiang and Y. Wang, *Biomaterials*, , DOI:10.1016/j.biomaterials.2010.09.068.

2   A. Aidun, A. Zamanian and F. Ghorbani, *Biotechnol. Appl. Biochem.*, , DOI:10.1002/bab.1694.

3   P. Lichte, H. C. Pape, T. Pufe, P. Kobbe and H. Fischer, *Injury*, , DOI:10.1016/j.injury.2011.03.033.

4   X. Wang, J. Shao, M. Abd El Raouf, H. Xie, H. Huang, H. Wang, P. K. Chu, X. F. Yu, Y. Yang, A. B. M. AbdEl-Aal, N. H. M. Mekkawy, R. J. Miron and Y. Zhang, *Biomaterials*, , DOI:10.1016/j.biomaterials.2018.06.039.

5   N. S. Nikonova, I. N. Tikhomirova, A. V. Belyakov and A. I. Zakharov, *Glas. Ceram. (English Transl. Steklo i Keramika)*, , DOI:10.1023/B:GLAC.0000008241.84600.f9.

6   M. Y. Shie, S. J. Ding and H. C. Chang, *Acta Biomater.*, , DOI:10.1016/j.actbio.2011.02.023.

7   L. Fei, C. Wang, Y. Xue, K. Lin, J. Chang and J. Sun, *J. Biomed. Mater. Res. - Part B Appl. Biomater.*, , DOI:10.1002/jbm.b.32688.

8   Y. Huang, C. Wu, X. Zhang, J. Chang and K. Dai, *Acta Biomater.*, ,

DOI:10.1016/j.actbio.2017.08.044.

9   H. Elsayed, J. Schmidt, E. Bernardo and P. Colombo, *Adv. Eng. Mater.*, , DOI:10.1002/adem.201801160.

10   P. Melo, A. M. Ferreira, K. Waldron, T. Swift, P. Gentile, M. Magallanes, M. Marshall and K. Dalgarno, *Compos. Sci. Technol.*, , DOI:10.1016/j.compscitech.2019.107834.

11   J. Xie, H. Shao, D. He, X. Yang, C. Yao, J. Ye, Y. He, J. Fu and Z. Gou, *MRS Commun.*, , DOI:10.1557/mrc.2015.74.

12   I. Tcacencu, N. Rodrigues, N. Alharbi, M. Benning, S. Toumpaniari, E. Mancuso, M. Marshall, O. Bretcanu, M. Birch, A. McCaskie and K. Dalgarno, *Mater. Sci. Eng. C*, , DOI:10.1016/j.msec.2018.04.022.

13   J. A. Sanz-Herrera, J. M. García-Aznar and M. Doblaré, *Acta Biomater.*, , DOI:10.1016/j.actbio.2008.06.021.

14   J. L. Drury and D. J. Mooney, *Biomaterials.*, , DOI: 10.1016/S0142-9612(03)00340-5.

15   D. M. Reffitt, R. Jugdaohsingh, R. P. H. Thompson and J. J. Powell, in *Journal of Inorganic Biochemistry.*, , DOI: 10.1016/S0162-0134(99)00126-9.

16   W. Sun, J. E. Puzas, T. J. Sheu, X. Liu and P. M. Fauchet, *Adv. Mater.*, , DOI:10.1002/adma.200600319.

17   A. S. Wagner, M. Schumacher, M. Rohnke, K. Glenske, M. Gelinsky, S. Arnhold, S. Mazurek and S. Wenisch, *Biomed. Mater.*, , DOI:10.1088/1748-605X/aaf701.

18   P. Y. Collart-Dutilleul, I. Panayotov, E. Secret, F. Cunin, C. Gergely, F. Cuisinier and M. Martin, *Nanoscale Res. Lett.*, , DOI:10.1186/1556-276X-9-564.

19   S. Kaihara, J. Borenstein, R. Koka, S. Lalan, E. R. Ochoa, M. Ravens, H. Pien, B. Cunningham and J. P. Vacanti, *Tissue Eng.*, , DOI:10.1089/107632700320739.

20   S. D. Gittard, A. Ovsianikov, B. N. Chichkov, A. Doraiswamy and R. J. Narayan, *Expert Opin. Drug Deliv.*, , DOI: 10.1517/17425241003628171.

21   J. Hernández-Montelongo, A. Muñoz-Noval, J. P. García-Ruíz, V. Torres-Costa, R. J. Martín-Palma and M. Manso-Silván, *Front. Bioeng. Biotechnol.*, , DOI: 10.3389/fbioe.2015.00060.

22   A. Di Luca, B. Ostrowska, I. Lorenzo-Moldero, A. Lepedda, W. Swieszkowski, C. Van Blitterswijk and L. Moroni, *Sci. Rep.*, , DOI:10.1038/srep22898.

23   V. Karageorgiou and D. Kaplan, *Biomaterials.* , , DOI: 10.1016/j.biomaterials.2005.02.002.

24   A. Seidi, M. Ramalingam, I. Elloumi-Hannachi, S. Ostrovidov and A. Khademhosseini, *Acta Biomater.*, , DOI: 10.1016/j.actbio.2011.01.011.

25   J. Kazantseva, A. Kivil, K. Tints, A. Kazantseva, T. Neuman and K. Palm, *PLoS One*, , DOI:10.1371/journal.pone.0074799.

26   J. Kazantseva, R. Ivanov, M. Gasik, T. Neuman and I. Hussainova, *Sci. Rep.*, , DOI:10.1038/srep30150.

27   T. Minasyan, L. Liu, M. Aghayan, L. Kollo, N. Kamboj, S. Aydinyan and I.

Hussainova, *Ceram. Int.*, , DOI:10.1016/j.ceramint.2018.04.208.

28   Z. Chen, X. Wu, D. Tomus and C. H. J. Davies, *Addit. Manuf.*, , DOI:10.1016/j.addma.2018.02.009.

29   N. Kamboj, M. Aghayan, C. S. Rodrigo-Vazquez, M. A. Rodríguez and I. Hussainova, *Ceram. Int.*, , DOI:10.1016/j.ceramint.2019.08.208.

30   C. Sarmento, Z. B. Luklinska, L. Brown, M. Anseau, P. N. De Aza, S. De Aza, F. J. Hughes and I. J. McKay, *J. Biomed. Mater. Res. - Part A*, , DOI:10.1002/jbm.a.30012.

31   N. Zhang, J. A. Molenda, S. Mankoci, X. Zhou, W. L. Murphy and N. Sahai, *Biomater. Sci.*, , DOI:10.1039/c3bm60034c.

32   I. Bružauskaitė, D. Bironaitė, E. Bagdonas and E. Bernotienė, *Cytotechnology.* , , DOI: 10.1007/s10616-015-9895-4.

33   J. R. Woodard, A. J. Hilldore, S. K. Lan, C. J. Park, A. W. Morgan, J. A. C. Eurell, S. G. Clark, M. B. Wheeler, R. D. Jamison and A. J. Wagoner Johnson, *Biomaterials*, , DOI:10.1016/j.biomaterials.2006.08.021.